

www.acsnano.org

Predicting Fracture Propensity in Amorphous Alumina from Its Static Structure Using Machine Learning

Tao Du, Han Liu, Longwen Tang, Søren S. Sørensen, Mathieu Bauchy,* and Morten M. Smedskjaer*



Cite This: ACS Nano 2021, 15, 17705–17716



Read Online

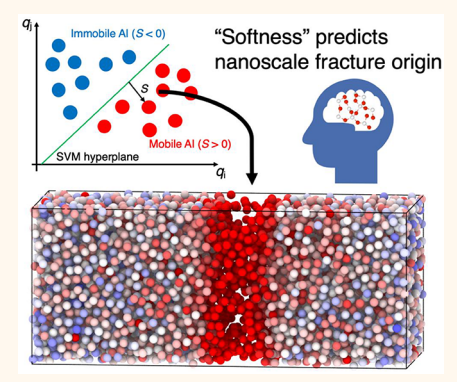
ACCESS

III Metrics & More

Article Recommendations

Supporting Information

ABSTRACT: Thin films of amorphous alumina (a-Al₂O₃) have recently been found to deform permanently up to 100% elongation without fracture at room temperature. If the underlying ductile deformation mechanism can be understood at the nanoscale and exploited in bulk samples, it could help to facilitate the design of damage-tolerant glassy materials, the holy grail within glass science. Here, based on atomistic simulations and classification-based machine learning, we reveal that the propensity of a-Al₂O₃ to exhibit nanoscale ductility is encoded in its static (nonstrained) structure. By considering the fracture response of a series of a-Al₂O₃ systems quenched under varying pressure, we demonstrate that the degree of nanoductility is correlated with the number of bond switching events, specifically the fraction of 5- and 6-fold coordinated Al atoms, which are able to decrease their coordination numbers under stress. In turn, we find that the tendency for bond switching can be predicted based on a nonintuitive structural descriptor calculated based on the static structure, namely, the recently developed "softness" metric as



determined from machine learning. Importantly, the softness metric is here trained from the spontaneous dynamics of the system (i.e., under zero strain) but, interestingly, is able to readily predict the fracture behavior of the glass (i.e., under strain). That is, lower softness facilitates Al bond switching and the local accumulation of high-softness regions leads to rapid crack propagation. These results are helpful for designing glass formulations with improved resistance to fracture.

KEYWORDS: amorphous oxides, molecular dynamics simulation, nanoductility, machine learning, fracture

xide glasses find a range of applications, from window panels and touchscreen displays to optical fibers for Internet communication and vaccine vials for fighting the COVID-19 pandemic. This is due to their desirable properties such as transparency, formability, thermal and chemical durability, and tailorable composition without stoichiometric requirements. However, oxide glasses are usually considered brittle, as they fracture catastrophically without plastic deformation at the macroscale, greatly hindering many applications. It is therefore essential to gain a deeper understanding of the deformation and fracture mechanisms of this material family.

In general, it is possible to induce brittle to ductile transitions in glasses and amorphous materials by tailoring their nanostructure through composition modification, 5-7 thermal treatment, 8,9 densification, 10 etc. In crystalline materials, fracture is affected by the competition between dislocations and bond breaking, with plasticity typically being initiated at defects. 5 However, the origin of ductility remains poorly understood in noncrystalline materials, since there are no well-defined defects in such materials due to the lack of

long-range-ordered structure. Even when the positions of all atoms in the static structure of a glass are fully known, it remains very challenging to identify the soft regions that are vulnerable to rearrangements. Several models have been proposed to account for the plastic properties of glasses, including elastoplastic, soft glassy rheology, and shear transformation zone (STZ)^{15,16} models. In metallic glasses, ductility is found to be related to the rearrangements of local structure, known as STZs. In contrast, the brittle nature of oxide glasses has been attributed to the lack of such regions of plastic deformation. Although these theories have proposed the existence of defects in the glass structure, they are unfortunately phenomenological and fail to provide a precise

Received: July 2, 2021
Accepted: October 27, 2021
Published: November 1, 2021





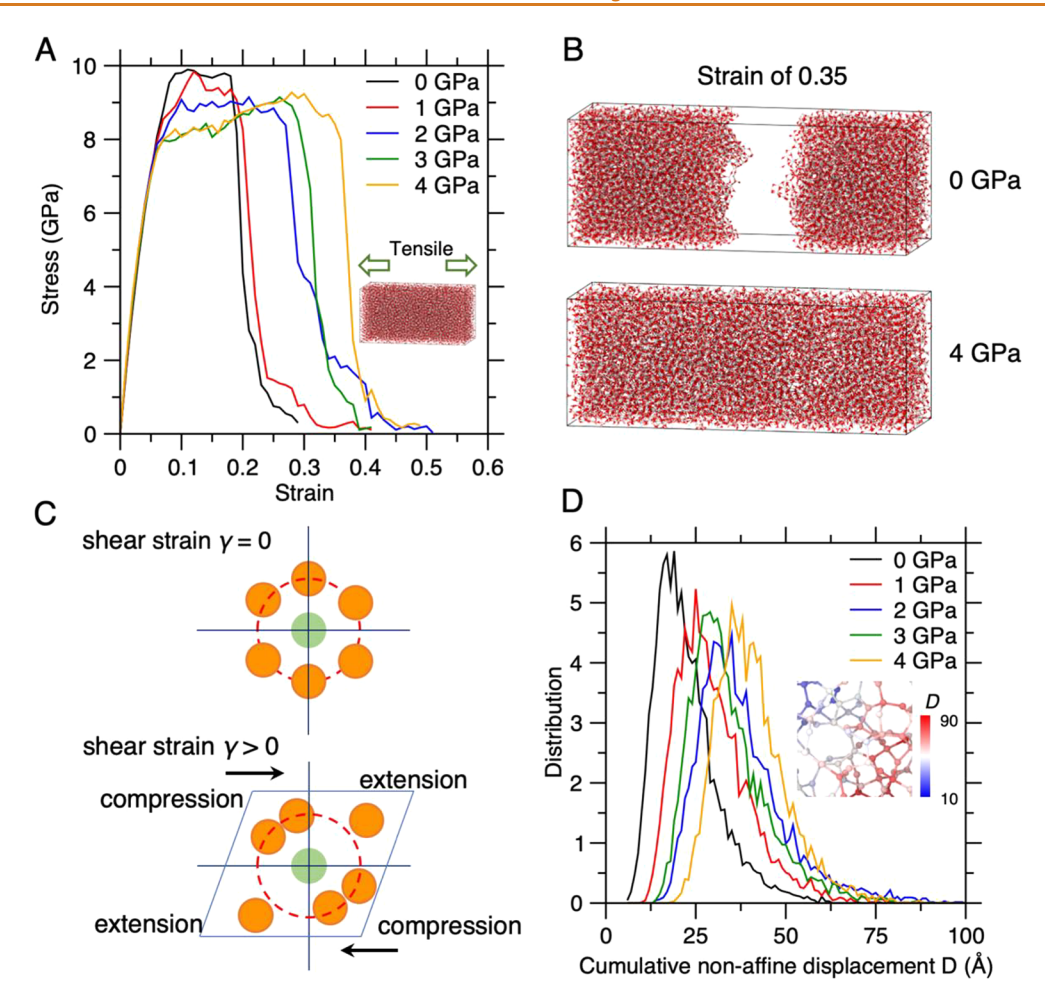


Figure 1. (A) Stress—strain curves of densified a-Al₂O₃ under the second loading condition (plane strain). (B) Atomic snapshot of a-Al₂O₃ at $\varepsilon = 0.35$. Al and O atoms are represented by white and red spheres, respectively. (C) Schematic showing the nonaffine displacement induced by applying a shear deformation γ . The nonaffine displacement of the central atom in green at strain γ is captured by the best-fit affine transformation of the neighboring atoms with reference to the initial configuration. (D) Distribution of the cumulative nonaffine displacement D of the Al atoms during the tensile process for the different densified a-Al₂O₃ samples.

definition of these defects, thus hindering their identification from first principles. ¹⁸ Recently, several data-driven models have been proposed to forecast the propensity of particles or atoms to rearrange. ^{19–22} However, due to the structural complexity of amorphous materials, the correlations between the structure and fracture mechanism in oxide glasses remain unknown.

To predict the tendency for crack propagation in oxide glasses based on their initial structure, it is necessary to first understand the correlation between structure and local atomic dynamics. Some structural descriptors such as local density, free volume, or bond orientational order can be correlated with flow defects, but are insufficient for fully predicting glass fracture.¹⁸ As a promising alternative path, advances within machine learning have made it possible to predict nonintuitive structural descriptors using algorithms such as support vector machine (SVM), ¹⁹ graph neural network, ²³ and convolutional neural network. ²⁰ Among these, the nonintuitive structural metric termed "softness" derived from SVM is found to be strongly correlated with the dynamics of specific atoms only based on their local structural environments. Note that although the order parameters used to construct the softness metric are simple two- and three-body order parameter terms, we refer to it as nonintuitive, as it is calculated from the

hyperplane constructed by the SVM classifier in the high-dimensional space formed by all the order parameters. Generally, the atoms with higher softness are more susceptible to rearrange or, equivalently, to be regarded as flow defects. The softness descriptor has been successfully adopted in understanding the dynamical heterogeneities at the glass transition, 22 creep dynamics of gels, 21 yielding behavior of disordered solids, 24 dynamics of grain boundaries in polycrystals, 25 thin film glass dynamics, 26 and crystallization kinetics at the solid—liquid interface. 27 Here, inspired by this approach, we explore whether the fracture behavior of amorphous oxides (which is governed by the local propensity of atoms to rearrange) is encoded in their static structure and whether the spontaneous dynamics (driven by temperature) has sufficient information encoded to predict the stress-driven dynamics during fracture.

By isolating nanoscale features of the glass structure that control the dynamics and mechanics of the macroscopic material, the era of nanoengineering of glasses could be unlocked, as inspired by the Materials Genome Initiative, ²⁸ in strong contrast to the traditional Edisonian trial-and-error approach for exploring composition—property relations. As an example, understanding the behavior of glasses at the nanoscale has been revealed to facilitate the fabrication of

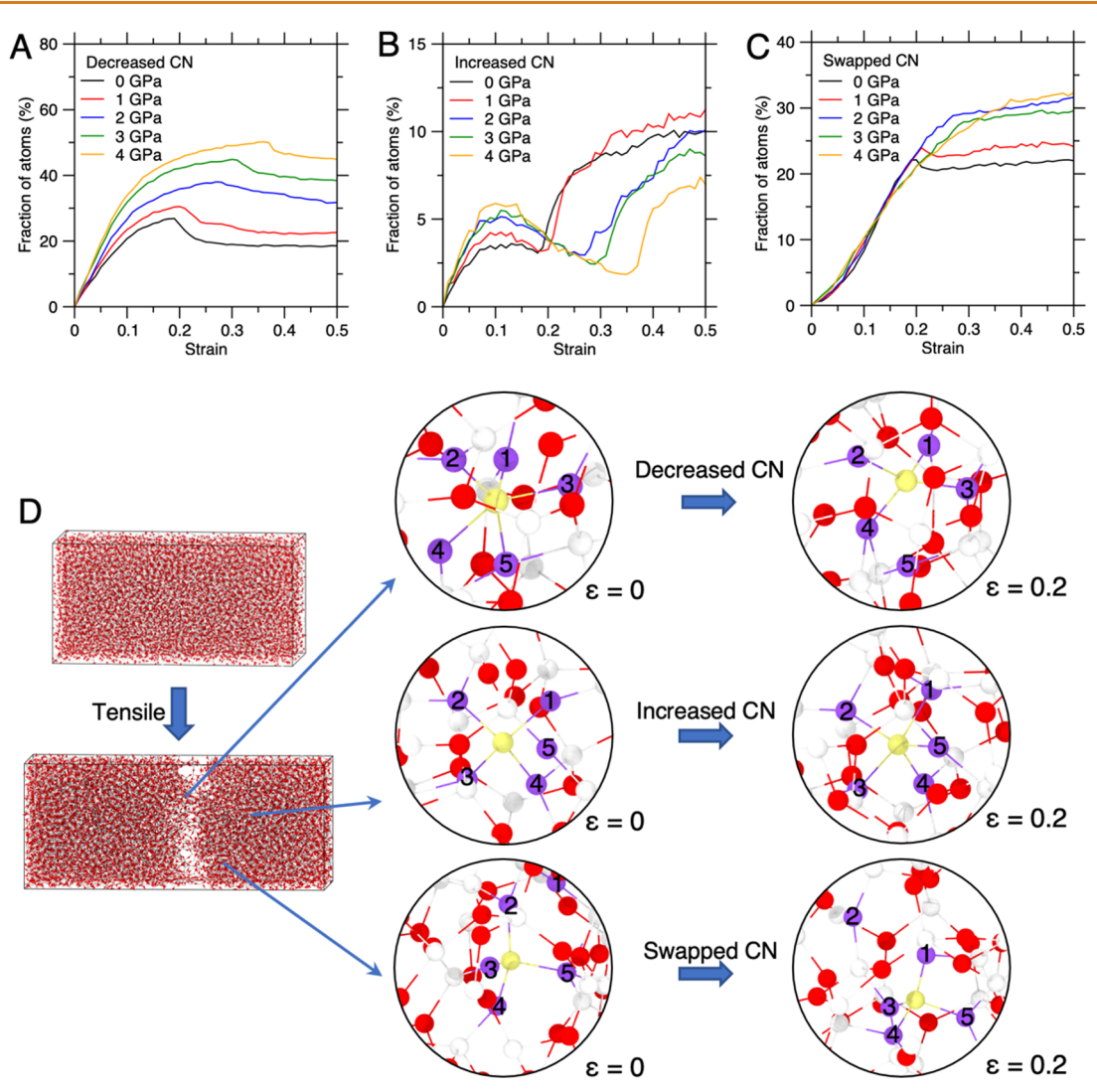


Figure 2. Fraction of Al atoms subjected to the bond switching activities under the second loading condition. (A) Decreased CN, (B) increased CN, and (C) swapped CN relative to the coordination environment in the nonstrained configuration. (D) Atomic snapshots of bond switching activities in a-Al $_2$ O $_3$ of 0 GPa upon tension. Top: Example of a decreased CN of Al (in yellow): The CN of Al is five at $\varepsilon = 0$ and decreases to four at $\varepsilon = 0.2$. Middle: Example of an increased CN of Al (in yellow): The CN of Al increases from four to five when ε increases from 0 to 0.2. Bottom: Example of a swapped CN of Al (in yellow) first connected to four O atoms (number 2, 3, 4, and 5) at $\varepsilon = 0$, but as ε increases to 0.2, the CN of Al remains four while connecting to a new O atom number 1.

glasses with enhanced plastic deformation. 29,30 Two other prominent examples include the fracture behaviors of amorphous alumina (a-Al₂O₃) and glassy silica at the nanoscale, which have been intensively studied. For silica, a brittle-to-ductile transition can be achieved through pressure quenching,¹⁰ reducing the sample size to the nanoscale,³¹ consolidating glassy nanoparticles, 32 or exposure to an electron beam.33 For a-Al₂O₃, depending on the loading conditions, some studies indicate plastic deformation at room temperature, 34-37 while others report a-Al₂O₃ to behave fully brittle. 38-40 Recently, pronounced plasticity in flaw-free thin films of a-Al₂O₃ at high strain rate has been attributed to a viscous creep mechanism, which is associated with Al bond switching events, i.e., decreasing or increasing coordination number and swapping of oxygen neighbors.³⁷ Such bond switching generates localized strain events, which accumulate into macroscopic flow. It is proposed that the bond switching activity leading to mechanical relaxation is more likely to occur in nanoscale alumina than in silica, partly due to the more

compact structure of a-Al $_2$ O $_3$ and its more accessible coordination states. Though the nanoscale plasticity in a-Al $_2$ O $_3$ has been ascribed to a viscous creep mechanism, the structural drivers for bond switching have not yet been revealed. This seriously limits our ability to exploit this mechanism of plasticity enhancement in bulk oxide glasses. That such exploitation at a larger scale is indeed possible has been highlighted in our recent study, where we reported a record-high fracture toughness (1.4 MPa m $^{0.5}$) in a bulk oxide glass with high propensity for bond switching. As such, an improved understanding of deformation and fracture mechanisms of glasses at the nanoscale is needed to improve their mechanical performance at the macroscale.

In this study, we investigate the structural origin of the ductile deformation behavior observed in a-Al $_2$ O $_3$. We do so in different pressure-quenched samples to vary the density, atomic structure, and thus propensity for bond switching. To obtain atomic scale information about the fracture mechanism, we use molecular dynamics (MD) simulations to

establish our conclusions since *in situ* mapping of atomic rearrangements during fracture is still out of reach experimentally. The densified a-Al₂O₃ samples are then subjected to uniaxial tension, and the fracture response is compared with bond switching analyses as well as the softness metric determined using SVM. We show that the degree of nanoductility in densified a-Al₂O₃ is related to the decrease in the coordination number of 5- and 6-fold coordinated Al atoms, with the fraction of these units increasing with a decrease in the average softness of Al atoms. Specifically, lower softness facilitates Al bond switching, and the local accumulation of high-softness regions leads to rapid crack propagation.

RESULTS AND DISCUSSION

Mechanical Response of Densified a-Al₂O₃. To obtain the data sets needed as input for machine learning, we first simulate the fracture behavior of densified a-Al₂O₃ samples under different loading conditions (see Methods section), since these conditions influence the simulated fracture response for a-Al₂O₃.³⁷ The stress-strain curves of a-Al₂O₃ under the first loading condition (plane stress) are shown in Figure S1. Consistent with ref 37, we find that a-Al₂O₃ exhibits a fairly ductile response under this loading condition. The total strain can reach values up to 50% without fracture for all the pressures used to predensify a-Al₂O₃. However, this makes it difficult to identify the differences in the ability of the densified a-Al₂O₃ samples to undergo plastic deformation. Therefore, we apply the second loading condition (plane strain), as shown in the inset of Figure 1A. The mechanical response is significantly influenced by the loading condition, with all the samples exhibiting a fairly brittle response, as manifested by a sudden drop in the stress-strain curve upon rapid crack propagation (see Figure 1A). We note that after reaching the first maximum stress, all the a-Al₂O₃ samples exhibit nearly constant stress with an increase in the strain before failure (i.e., yielding regime) due to the existence of plastic deformation. Importantly, with an increase in the pressure during quenching, the yielding regime becomes more pronounced, showing that the more densified a-Al₂O₃ samples feature improved nanoductility (see Figure 1B). Atomic snapshots of the fracture evolutions of a-Al₂O₃ samples densified at 0 and 4 GPa are shown in Figure S2. We note that densificationinduced nanoductility has also been observed in amorphous silica.10

We then calculate the cumulative nonaffine displacement (D) of each Al atom (see Methods section) to understand the carriers of plasticity during fracture under the second loading condition (plane strain). Since D represents the irreversible structural rearrangements of each atom, it has been successfully applied to identify the activation of STZs of various amorphous systems during fracture. 42 Figure 1C illustrates how the nonaffine displacement captures the rearrangement of the particles by isolating the nonaffine motion associated with local rearrangements from the best-fit affine deformation of its neighborhood. As shown in Figure 1D, we observe that with an increase in pressure during quenching, the Al atoms tend to have larger values of D, indicating an increasing extent of structural reorganization during the fracture process. Since the nonaffine displacement reflects the plasticity events of the atoms under stress,⁴² densification of a-Al₂O₃ improves the nanoductility by facilitating nonaffine reorganizations of the Al atoms. This is reflected through the linear growth of plastic

energy with the cumulative nonaffine displacement D of Al atoms as shown in Figure S3.

Stress-Induced Bond Switching Events. In the following, we analyze the bond switching activities as a function of strain to correlate the nonaffine reorganizations with the bonding state of Al atoms. The bond switching activities are defined as the changes in the coordination environment of the Al atom, i.e., whether the coordination number (CN) decreases or increases or if a neighbor oxygen is swapped by another one compared to the nonstrained configuration. As shown in Figure 2A-C, the extent of all three bond switching events increases with an increase in strain. This indicates that structural reorganizations can be achieved though bond switching, which dissipates the strain energy during fracture.⁴¹ When comparing the extent of bond switching events under the two different loading conditions, we find the main difference to be the fraction of swapped CN at the final strain of 0.5 (see results for the first and second loading condition in Figure S4C and Figure 2C, respectively). That is, the final swapped CN fraction is in the range of 40-55% and 20-35% for the first and second loading condition, respectively. We also observe that the pressure dependence of the swapped CN fraction in the two loading conditions is inverse, indicating that the swapped CN is related to the loading conditions. This is due to the fact that all the bond switching events facilitate nanoductility by allowing the structure to reorganize instead of allowing crack propagation. For the first loading condition (plane stress), all samples exhibit the same nanoductility by having almost the same number of bond switching events (around 90% when considering all the bond switching events). When the sample is quenched at a higher pressure, the overcoordinated Al atoms are more prone to decrease their CN upon deformation. Consequently, samples quenched at high pressures have a lower fraction of the swapped CN events under the first loading condition.

Since the fraction of decreased CN is enhanced by densification for both loading conditions (see Figures 2A and S4A), we infer that the pressure-induced plasticity can be associated with the activities related to decreased CN. The accumulated rise in the decreased CN activities in the densified a-Al₂O₃ implies that more potential energy has been dissipated through the breakage of Al-O bonds, which allows for less stress accumulation in the glass during tensile loading and thus improves nanoductility. In the remaining part of this paper, we will focus on understanding the structural origin of the densification-induced nanoductility in a-Al₂O₃ for the second loading condition (plane strain), for which the largest differences in fracture response are observed. The atomic snapshots of Al atoms undergoing three bond switching activities at $\varepsilon = 0.2$ are shown in Figure 2D. For the a-Al₂O₃ sample quenched at 0 GPa, we observe that a crack has already propagated at ε = 0.2. By analyzing the bond switching activities, we find that Al atoms undergoing decreased CN and swapped CN are mainly located in the vicinity of the crack, highlighting the spatial distribution of bond switching activities.

The initial configurations of the a-Al $_2$ O $_3$ samples are affected by the applied pressure, which in turn impacts the fracture response. To investigate this, we first compute the CN of Al atoms of the nonstrained structure and classify them into decreased CN, increased CN, and swapped CN based on the bond switching activities at a strain of 50%. We first observe that the CN states of Al atoms are significantly influenced by

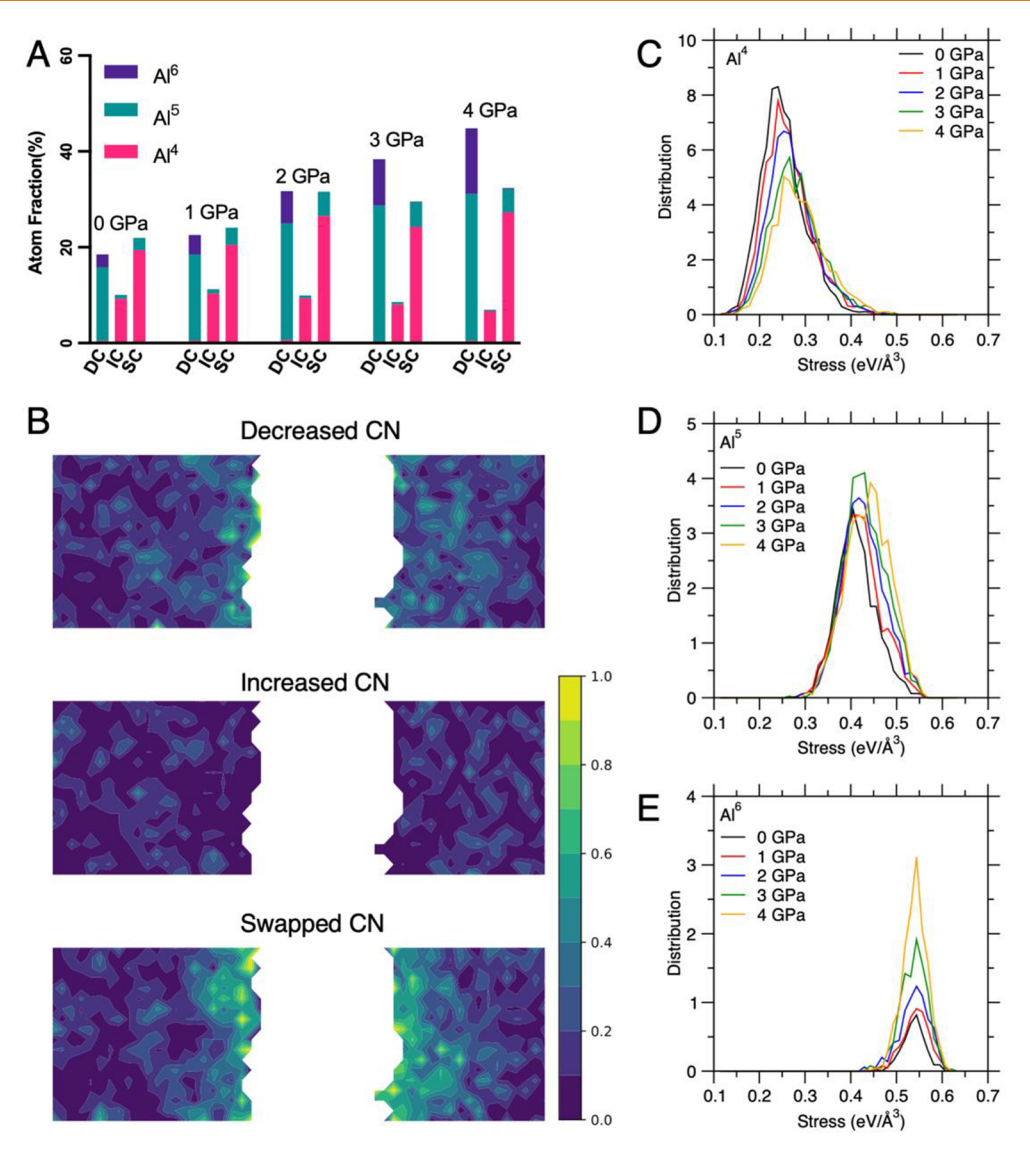


Figure 3. (A) Fractions of different Al species subjected to bond switching activities upon fracture in the five different densified samples. Here, DC, IC, and SC represent decreased CN, increased CN, and swapped CN, respectively. (B) Spatial distribution of the normalized fraction of Al atoms with decreased CN, increased CN, and swapped CN. The calculations are based on a-Al₂O₃ formed under 0 GPa at ε = 0.5. (C, D, E) Distribution of the local stress undergone by (C) Al⁴, (D) Al⁵, and (E) Al⁶ atoms under different pressures. The distributions of these different Al species are normalized by the total number of Al atoms.

the applied pressure. The fractions of 5-fold Al atoms (Al⁵) and 6-fold Al atoms (Al⁶) increase at the expense of 4-fold Al atoms (Al⁴) with an increase in the quenching pressure (Figure S5). Notably, we observe that the initial state of Al atoms significantly influences the bond switching activities during fracture. Specifically, Al⁶ species exhibit the largest degree of decreased CN, while Al⁴ species exhibit the largest degree of increased or swapped CN upon fracture (Figure 3A). This can be understood from the fact that Al⁶ units are formed due to the application of pressure during cooling, but remain stuck in their overcoordinated state during the final zero pressure relaxation. At this point, these overcoordinated units are in a metastable equilibrium state. The following application of a tensile stress then allows them to quickly relax toward the more stable 5- or 4-fold coordinated states while dissipating energy within the structure. Based on the bond switching results under two loading conditions (Figures 2A and S4), the pressure-induced nanoductility is mainly attributed to the decreased CN of Al5 and Al6 atoms, as the fractions of Al6 and

Al⁵ species that decrease their CN increase with increasing pressure (Figure 3A).

Next, we analyze the spatial distribution of various bond switching events (decreased, increased, and swapped CN for Al atoms) in a-Al₂O₃. As shown in Figure 3B, bond switching events in the sample quenched at 0 GPa mainly occur near the fracture surface, with only a few structural arrangements occurring in the bulk glass. Considering the spatial distributions shown in Figure S6 for the other samples, we find that the distributions of decreased CN (DC) and swapped CN (SC) are influenced by the applied quenching pressure. Specifically, DC and SC events tend to concentrate near the fracture surface and more DC and SC events occur in the bulk glass with an increase in pressure. This allows for local structural arrangements to dissipate stress during the fracture process. However, the distribution of increased CN (IC) events shows a uniform distribution in the bulk glass despite the change in pressure. Overall, these results suggest densified

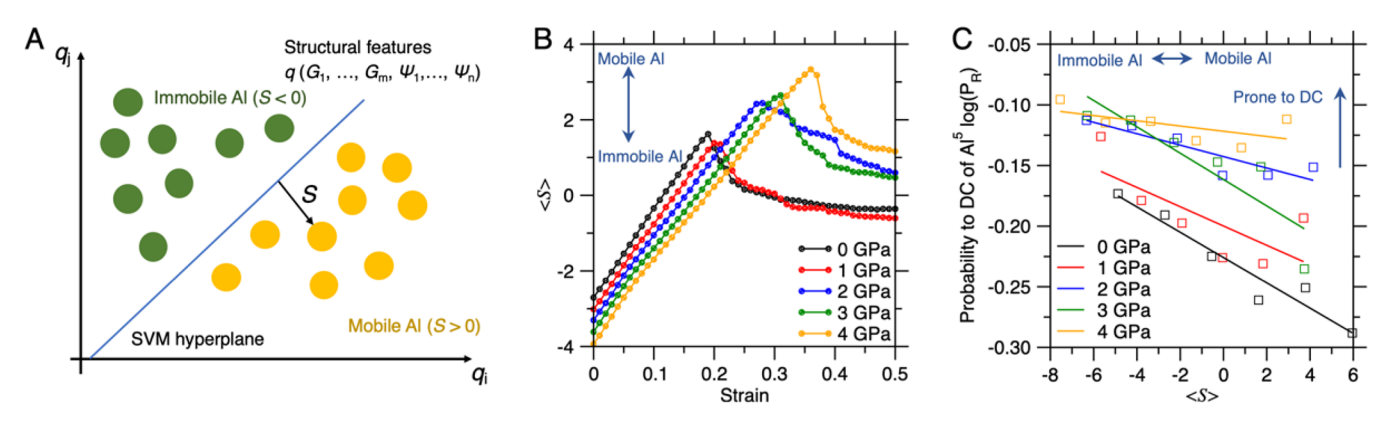


Figure 4. (A) Illustration of the classifier model used to distinguish mobile Al atoms (in yellow) and immobile Al atoms (in green) through a SVM hyperplane (blue line). The input features are constructed by a combination of radial and angular structure functions (see eqs 4 and 5) to describe the local environment of each Al atom. (B) Average softness of Al atoms as a function of the applied strain in the different densified a-Al₂O₃ samples. (C) Probability of Al⁵ to decrease its CN during fracture as a function of the average softness $\langle S \rangle$ in the static (nonstrained) a-Al₂O₃ samples.

 $a\text{-}Al_2O_3$ facilitates more structural rearrangements to increase its nanoductility.

To describe the formation mechanism of the various types of Al coordination states, we calculate the local stress experienced by the Al atoms in the different samples. As shown in Figure 3C, we observe that these internal stresses are influenced by the applied pressure during quenching. With an increase in pressure, the stress experienced by Al⁴ and Al⁵ atoms increases, which is a consequence of their decrease in Voronoi volume under higher pressure. However, for Al⁶ atoms, there is no significant pressure-induced shift in the stress distribution. Consistent with the results from ref 43, we thus find that the stress on Al increases with CN. This indicates that the maximum stress experienced by each Al atom is related to their CN and, as the pressure increases, Al atoms will gradually increase their CN in order to balance the external pressure during quenching, eventually forcing these Al atoms to remain in their overcoordinated state even after the 0 GPa relaxation. When the system is under plastic deformation, the CN of Al atoms will change in order to balance the external stress. The relationship between CN and stress of Al atoms indicates that Al atoms undergo DC events, which effectively release the atomic stress. Furthermore, as 7-fold Al atoms are not observed, we deduce that an increase in pressure can increase the fraction of Al⁶ without influencing the stress distribution. Although the pressure-induced formation of Al⁶ species can increase the extent of DC events, the most important source of DC events is from Al⁵ species. As shown in Figure S7, the stress on Al⁵ atoms in the 0 GPa sample undergoing DC events is in the same range as that of the non-DC events (IC, SC, and unchanged CN). Hence, the bond switching behavior of Al⁵ atoms cannot be directly related to the stress analysis.

Atom Mobility Classification by Machine Learning. As described above, the bond switching behavior of Al atoms (especially Al⁵ atoms) cannot be directly related to intuitive structural descriptors of the nonstrained glass structure, such as coordination numbers, atomic stress, position, *etc*. We therefore adopt the machine learning-based softness metric to investigate whether the mobility of Al atoms and thus their ability to promote plasticity could be encoded in a nonintuitive manner in the spontaneous dynamics of the initial (*i.e.*, unstrained) amorphous structure. We also seek to explore how the mobility of Al atoms is related to the bond switching events

under stress. To this end, we first build the SVM hyperplane (see schematic in Figure 4A) based on the initial structure of all the a-Al₂O₃ configurations before any load is applied (see Methods section for details). As expected, the classification accuracy greatly depends on the structural input used for training. In detail, when solely relying on radial functions, the classification accuracy can reach 79% (see Figure S8), with the first peak of the Al-O pair having the largest contribution to the classification as seen from Figure S9. Notably, we find that this classifier can properly classify the Al atoms as mobile or immobile with an accuracy of 84% and 83% for the training and test data sets, respectively, with the structural input features of radial and angular functions. We also attempted to include the atomic Voronoi volume as an input feature. However, when trained solely on the Voronoi volume, the classifier yields an accuracy of 56%, which is considerably lower than using the structural functions. We also notice that the accuracy of the classifier does not increase when including both Voronoi volume and structural functions as input, indicating that the latter already includes the knowledge of Voronoi volume (see Figure S8). We find that the correlation between softness and Voronoi volume is related to the CN of Al atoms. That is, the Voronoi volume decreases with an increase in the CN of the Al atoms. For Al⁴ and Al⁵ atoms, the Al atoms with larger Voronoi volumes tend to have lower softness (see Figure S10). This may seem counterintuitive, as larger available free volume should be associated with larger propensity to rearrange and thus higher softness. However, we ascribe this to how the Al⁴ and Al⁵ atoms with large Voronoi volumes are in a metastable equilibrium state of Al⁴-to-Al⁵ and Al⁵-to-Al⁶ transitions, respectively, which are prone to rearrange over time. When the amorphous structures are under tension (e.g., ε = 0.1), the softness increases with an increase in the Voronoi volume, but the correlation between softness and Voronoi volume remains the same as in the nonstrained state. This suggests that even though softness is largely dependent on the Voronoi volume, the other structural features are more influential. Moreover, we cannot find a strong correlation between softness and CN (see Figure S11).

Then, we calculate the softness of each Al atom based on the structural descriptors of Al generated from the configurations at every strain step. This in done in order to investigate the relationship between softness and the fracture process of a-

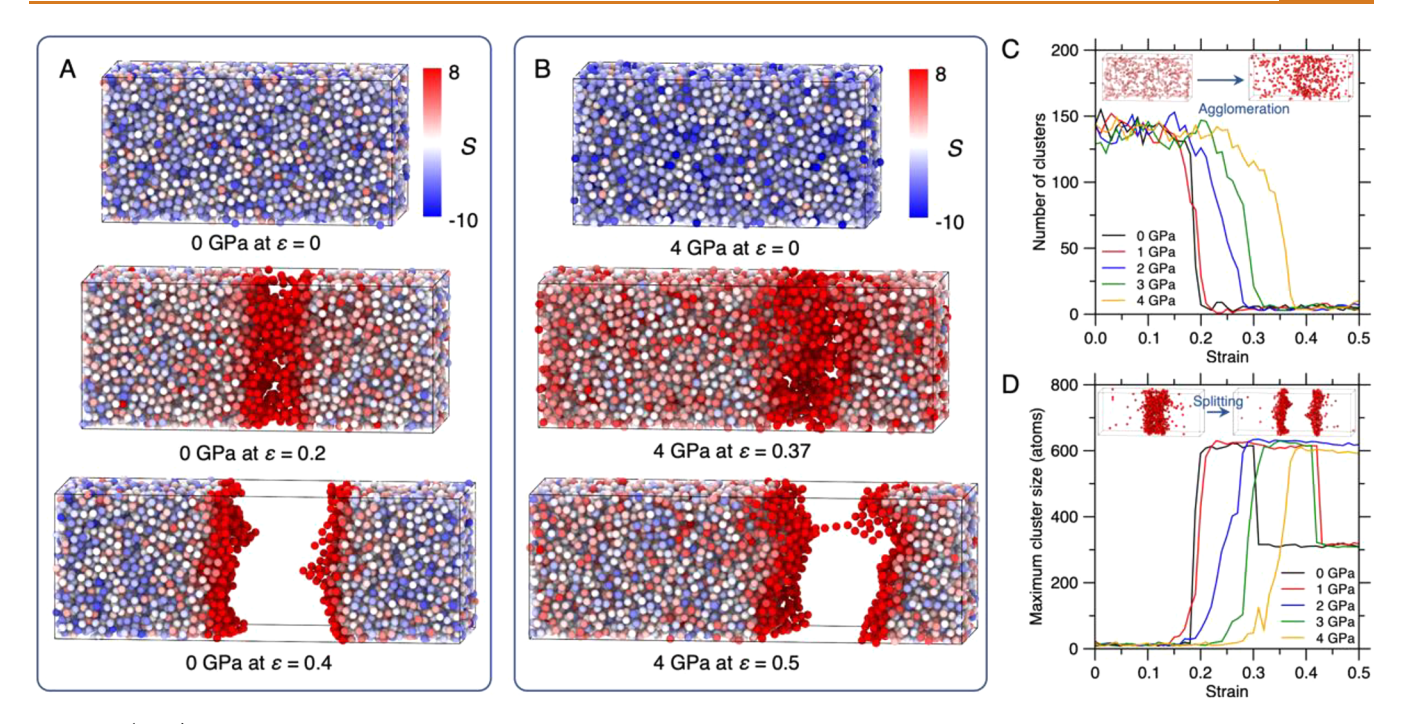


Figure 5. (A, B) Atomic snapshots of $a-Al_2O_3$ during the fracture process, where the Al atoms are visualized colored according to their softness (S). Samples quenched at 0 and 4 GPa are shown in (A) and (B), respectively. (C) Number and (D) maximum size of the high-softness clusters as a function of the applied strain in the different densified $a-Al_2O_3$ samples. The inset figures in (C) and (D) show the agglomeration and splitting, respectively, of the high-softness Al atoms.

 Al_2O_3 . We first evaluate how the average softness $\langle S \rangle$ of the system (i.e., averaged over all the Al atoms) evolves during fracture (Figure 4B). Overall, we find that $\langle S \rangle$ exhibits an increase with the applied strain to a maximum value followed by a drop for all the a-Al₂O₃ samples. Compared with the stress-strain curves in Figure 1A, we observe that the strain at the maximum $\langle S \rangle$ agrees well with the strain for which stress starts to decrease rapidly, i.e., the onset of crack propagation. Furthermore, we note that the slope of the softness vs strain curve up to the maximum $\langle S \rangle$ varies with the strain value, which can be correlated to the mechanical response. Specifically, as shown in Figure S12, the slopes are all in the range of 18-26, but can be roughly divided into three different regions depending on the strain. In the first region, the slope is relatively constant or slightly increasing with strain in the elastic region (ε < 0.07). In the second region, the slope rapidly decreases with strain until the structure fully enters the yield region (0.07 < ε < 0.09), which reflects the initiation of plastic regions. At higher strain, the slope increases with some fluctuations, corresponding to the plastic deformation and crack formation in the structure. Based on these results, softness can also capture the early stage mechanical response under deformation. This indicates that the dynamics of rearrangement at the nanoscale can be captured by the atom-level softness metric (see Figure S13). We also note that the decrease of $\langle S \rangle$ continues after full fracture, which can be related to the relaxation of the glass, e.g., an increasing amount of IC events, even following fracture (see Figure 2B).

Interestingly, we also observe that the quenching pressure influences the evolution of $\langle S \rangle$ with strain. For the nonstrained configurations, $\langle S \rangle$ exhibits a decrease with increasing pressure as the more compact network will give rise to atoms with lower mobility (*i.e.*, lower S). The distribution of S in the nonstrained structures also suggests an increasing amount of Al atoms with

lower S induced by densification (see Figure S14A). When strain is applied, $\langle S \rangle$ grows monotonically with strain until the maximum value, indicating that upon tensile deformation, the atoms gradually become "softer" and more prone to reorganization. In contrast, the maximum $\langle S \rangle$ during fracture increases with increasing pressure, indicating that the originally "hard" atoms (i.e., less mobile) can absorb more energy and become activated into "soft" atoms with high mobility. However, when "soft" atoms absorb energy, they are more likely to transform into irreversible defects, e.g., the undercoordinated Al atoms, which exhibit a long tail toward high softness in all the samples upon fracture (see Figure S14B). We have also observed that the initially "harder" atoms are more likely to transform into "soft" atoms upon deformation (see Figure S15), indicating that the less mobile atoms are the reservoir of nanoductility. This is consistent with recent work showing that atoms with high self-adaptivity (and thus apparently low softness) under stress can help to suppress crack formation.44

Linking Atom Dynamics to Bond Switching and Fracture. To further establish the relationship between the initial equilibrium, nonstrained structure, and the long-term far-from-equilibrium fracture response, we combine the concepts of bond switching and softness to explore the link between the dynamics of the atoms and their propensity to undergo bond switching. Based on the results of Figure 2A, the nanoductility of a-Al₂O₃ is closely related to the events of decreasing CN of Al⁵ atoms. As such, we have calculated the probability of Al⁵ to decrease its CN (P_R) during the entire fracture process. This calculation is achieved by grouping the Al⁵ atoms with similar softness and extracting the fraction of DC events at $\varepsilon = 0.5$. We do so to explore the relationship between P_R and the softness of the nonstrained configurations. As shown in Figure 4C, we find that P_R exhibits an

approximate exponential dependence on $\langle S \rangle$, and with a decrease in $\langle S \rangle$, the Al⁵ atoms tend to decrease their CN rather than other bond switching behaviors. This correlation is significant, as it highlights that the far-from-equilibrium response of the glass upon fracture is largely encoded in its static, unloaded structure. The exponential dependence of $P_{\rm R}$ on the softness metric S can be reminiscent of an activated process as suggested elsewhere, 21 with softness acting as an effective activation energy for Al⁵ atoms to decrease their CN. The transformation from "hard" to "soft" atoms occurs continuously upon straining and is accompanied by the energy-absorbing bond switching activities. Combined with the results in Figure S15, we conclude that Al atoms with lower S will experience a larger softness increase after fracture, which agrees with the fact that the DC events are the most energy consuming bond switching activities. This can also be understood from the fact that Al atoms with lower S are typically under higher atomic stress, while DC activity can effectively release the atomic stress based on the results shown in Figure 3C. We also observe an increasing probability of Al⁵ to decrease CN in a-Al₂O₃ samples quenched at higher pressure, suggesting that this bond switching event of Al⁵ is determined by the softness of the whole system. Based on the results of ref 21 the energy barrier of DC activity becomes lower with increasing quenching pressure. Interestingly, as $\langle S \rangle$ of the whole system decreases (for increasing quenching pressure), the dependence of P_R of Al⁵ to decrease its CN on individual softness becomes less significant (Figure 4C).

Since the evolution of average softness can capture the crack propagation, we now investigate the linkage between the distribution of softness and the corresponding fracture states. To this end, we select two systems with widely different degrees of nanoductility, namely, the samples quenched at 0 and 4 GPa, to investigate the evolution and the spatial distribution of softness during different fracture stages (nonstrained state, just prior to fracture, and after fracture, respectively). As shown in Figure 5A,B, we observe that a-Al₂O₃ quenched at 4 GPa has lower initial softness than the 0 GPa sample. Upon tension, the softness of each atom increases monotonically, and most of the atoms with high softness (redcolored spheres) accumulate in a band when the system is about to fracture. The location of the band is found to be related to the origin of fracture, where the atoms exhibit large Voronoi volumes. The bandwidth in a-Al₂O₃ quenched at 4 GPa is larger than that in the 0 GPa sample, leading to a more rough fracture surface in a-Al₂O₃ quenched at 4 GPa upon fracture, as also reflected in more surface area created by fracture (see Figure S16).

For comparison, we also attempt to use Voronoi volume as an indicator of crack propagation. To this end, we track the evolution of softness and Voronoi volume of Al atoms during the loading process. We randomly select Al atoms with different locations (away from the crack and in the crack) as shown in Figure S17 and observe that softness features an increasing and then decreasing trend with strain for all the Al atoms (similarly to what is shown in Figure 4B). However, the Voronoi volume does not systematically follow the same trend, indicating that the increase of softness is not only due to the formation of cavities. We have also investigated the clusters of high-volume atoms, observing that the atom with a high atomic volume does not ensure a high softness (see Figure S18). Although the high-volume atoms also agglomerate upon fracture, the locations of high-softness atoms are more

concentrated on the crack initiation region, as also reflected by the formation of more clusters with smaller sizes upon fracture. These results suggest that the softness metric can be used to predict fracture propensity. That is, although the softness metric is trained based on the static structure prior to any applied stress, the spatial distribution of softness can capture the initiation as well as the propagation of a crack during fracture.

We further investigate the clustering behavior of highsoftness Al atoms to understand the relationship between the location of high-softness Al atoms and growth of the crack during fracture. As shown in Figure 5C, we observe that initially (at low strain) the high-softness atoms are uniformly distributed in the matrix regardless of the densification degree. This is based on the fact that the constant number of 648 highsoftness Al atoms are distributed in around 120 clusters. Upon fracture, the number of high-softness clusters significantly decreases. The samples with a more nanoductile fracture response exhibit a decrease in the number of clusters at a relatively higher strain. Figure 5D shows the maximum size of the high-softness clusters during the fracture process. The strain at which the maximum cluster size starts to increase corresponds to the drop in stress in the stress-strain curves (Figure 1A) after the crack starts to propagate. The maximum high-softness cluster size for all the systems is about 600 atoms, which is almost equal to the number of high-softness atoms, showing that most of the high-softness atoms agglomerate during fracture. As expected, the end of fracture is also captured by this quantity as a sudden drop of the maximum cluster size, as the cluster is split into two smaller clusters once the sample is fully fractured.

CONCLUSIONS

In this work, we have identified the origin of the nanoductility in densified a-Al₂O₃ samples by establishing the correlation between the initial static structure and dynamics captured by the so-called "softness" metric, local bond switching events, and the long-term fracture behavior. We find that the origin of nanoductility can be attributed to the increased amount of Al⁵ and Al6 atoms in the densified samples that have high propensity to decrease their coordination number during fracture. On the basis of classification-based machine learning calculations, we reveal that the long-time dynamics of the atoms upon fracture are hidden in the initial static structure of a-Al₂O₃, before any load is applied. Although the machine learning model is trained based on the spontaneous dynamics, it properly captures the far-from-equilibrium dynamics upon loading. This approach thus allows us to predict the propensity for crack propagation in a realistic disordered oxide based solely on the machine-learned softness metric. In the present case, we show that almost all the Al⁶ and Al⁵ atoms with lower softness atoms tend to decrease their coordination numbers during fracture. Our results also suggest that the formation of high-mobility regions leads to the failure of the system. On the basis of these observations, we envision that machine learning can help to decode the hidden correlations between nanoscale structural features and mechanical properties in disordered materials and consequently help to design tougher oxide glasses by rational design of the atomic structure.

METHODS

Sample Preparation. In this study, we adopted the Large-scale Atomic/Molecular Massively Parallel Simulator (LAMMPS) soft-

ware⁴⁵ to perform MD simulations of a-Al₂O₃ with the classical potential of Matsui,⁴⁶ which has been widely used in reproducing the structure and mechanical properties of various phases of Al₂O₃.^{37,47-49} The long-range Coulombic interactions were calculated using the particle—particle—mesh (PPPM) method with an accuracy of 10^{-5} .⁵⁰ The motion of atoms was described by the velocity-Verlet integration algorithm with a time step of 1 fs. A Nosé—Hoover thermostat and barostat were applied to control the temperature and pressure, respectively, when applicable. Periodic boundary conditions were applied in all directions.

We generated the a-Al₂O₃ configurations through the process introduced by Gutiérrez *et al.*⁴⁹ Specifically, 1620 Al₂O₃ units (8100 atoms) were placed in an orthorhombic box at a density of 2.75 g/ cm³. Then the systems were melted in the NVT ensemble at 5000 K for 45 ps to ensure the loss of any memory of the initial structure. Afterward the structure was cooled to 3000 K for 10 ps and further equilibrated at 3000 K for 45 ps. The density of the system was changed to 3.175 g/cm³ and equilibrated for an additional 45 ps in the NVT ensemble. The next step was to cool the system to 300 K in the NPT ensemble under different pressures (0, 1, 2, 3, and 4 GPa, respectively) over 650 ps. The systems were then successively relaxed in the NVT and NPT ensembles at 300 K and 0 pressure for another 35 ps. This process of cooling from high temperature also ensures that the samples quenched from different pressures are independent of each other, since the high-temperature melting removes any memory of the initial structure. The utilized cooling and relaxation processes were adopted from ref 37 and found to be long enough to reproduce the material properties of a-Al₂O₃. The structure of a-Al₂O₃ quenched at 0 GPa after relaxation is shown in Figure S19A. Although the glasses were eventually relaxed at zero pressure, the densification during quenching was permanent since the system remains frozen in its densified state once it reaches the glassy state. As shown in Figure S19B, the applied pressure can effectively densify the a-Al₂O₃ structure, with a linear increase in density with pressure.

Fracture Simulations. The deformation and fracture behavior of a-Al₂O₃ was analyzed by applying a uniaxial tensile deformation. We note that the fracture behavior of a-Al₂O₃ strongly depends on the loading conditions as mentioned in ref 37. Here, we applied two tensile protocols to systematically investigate the effect of loading mode on fracture. Before the tensile simulations, the orthorhombic a-Al₂O₃ configurations were duplicated in the *x*-direction so that the loading was applied to the longer direction. The resulting structures (consisting of 16 200 atoms) were equilibrated at 300 K and zero pressure in the *NPT* ensemble for 100 ps before deformation.

The first loading condition was adopted from ref 37. Specifically, a constant strain rate of $5 \times 10^{10} \, \mathrm{s}^{-1}$ was applied along the *x*-direction, while the barostat was used to keep the lateral directions at zero stress (*i.e.*, "plane stress" conditions). During the tensile simulation, the system was maintained at 300 K. The duration of the tensile simulation was 1 ns, leading to a total strain of 50%. The stress–strain curve was constructed based on the stress component in the *x*-direction and corresponding strain.

The second loading condition was adopted from ref 42. In this loading mode, the system along the *x*-direction was deformed by small strain steps of 1%, while the sizes in lateral directions were fixed (*i.e.*, "plane strain" conditions). At each step of deformation, the structure was subjected to an initial energy minimization and then equilibrated in the *NVT* ensemble at 300 K for 10 ps before sampling the stress. This procedure was iteratively repeated until the structure was fully fractured.

Cumulative Nonaffine Displacement D. The cumulative nonaffine displacement D of each Al atom upon loading was computed to investigate the irreversible structural rearrangements, which were responsible for the plasticity during the fracture process. D has previously been successfully applied in capturing the number and magnitude of the local plastic events occurring in the atomic structure during fracture processes. This concept originates from the nonaffine square displacement D_{\min}^2 , which has been widely used in identifying the activation of STZs upon deformation. The quantity D_{\min}^2 describes the degree of local reorganization of atoms

by subtracting the displacement induced by the affine deformation of the simulation box. The degree of local reorganization of each atom in the strained configuration can be quantitatively measured by comparing with the nonstrained configuration. However, since the configuration will experience significant changes once fractured, we instead used a cumulative nonaffine displacement D, which accounts for the entire fracture process by properly considering the local ductile events. This quantity is calculated by summing up the nonaffine displacements at each small strain step s:

$$D = \sum_{s=1}^{n} \sqrt{\Delta D_{s,\min}^2} \tag{1}$$

where $\Delta D_{s,\min}^2$ is the incremental nonaffine square displacement with each increment of strain s and n is the total number of strain steps. The cutoff used for the calculation of $D_{s,\min}^2$ was set to 4 Å, which covers the first and second coordination shells of Al atoms.

Local Atomic Stresses. We calculated the local stress experienced by each Al atom by adopting the formalism of "stress per atom". ⁵² Note that, strictly speaking, stress is ill-defined for individual atoms and can only be meaningful when calculated for an ensemble of atoms. To overcome these difficulties, we here adopt the concept of "stress per atom" introduced by Egami, ⁵³ wherein the local atomic local stress tensor $\sigma_i^{\alpha\beta}$ is defined by expressing the contribution of each atom i to the virial of the system,

$$\sigma_i^{\alpha\beta}V_i = \sum_j r_{ij}^{\alpha} \cdot F_{ij}^{\beta} \tag{2}$$

where V_i is the volume of atom i, r_{ij} and F_{ij} are the distance and interatomic force, respectively, of atom j applied to atom i, and the indices α and β represent the projections of these vectors along the α , α , and α directions. The volume α of each atom was calculated based on the Voronoi tessellation. The local hydrostatic stress undergone by each atom can be calculated by the trace of the stress tensor. By convention, a positive stress denotes a state of local tension, while a negative one refers to a state of compression. The presence of local atomic stress does not imply that the system is under any macroscopic stress, namely, some atoms are locally under compression whereas others are locally under tension and eventually mutually compensate each other so that the whole system can still remain under zero pressure. This formalism has previously been successfully adapted to amorphous materials.

Coordination Number and Bond Switching Analyses. During the fracture process, plasticity is associated with the atomic arrangements that occur due to bond breaking and re-formation. We have thus analyzed the changes in coordination number and bond switching activities as a function of the applied tensile strain. To analyze the CNs, we first calculated the partial pair distribution functions. The cutoffs between Al and O were selected to be the distance at the minima after the first peak in the pair distribution function. To this end, partial pair distribution functions of Al—O and Al—Al are shown in Figure S20. The atoms of Al and O are considered bonded if they are within the cutoff. The cutoff selected in this study was 2.25 Å for Al—O pairs, and the CN of Al was defined as the number of O atoms within this cutoff.

The bond switching analysis was carried out by comparing the CN and the identity of the neighboring atom of each individual atom with its initial nonstrained structure. If the CN has decreased or increased, then the atoms were labeled as DC or IC, respectively. If both the CN and the neighboring atoms remain unchanged, then the atoms were labeled as UC. Otherwise, the atoms were counted as SC, indicating the unchanged CN with at least one different neighboring atom. A schematic illustration of these different bond switching events is shown in Figure S21. Note that the time intervals (2 ps) or strain step (0.01) of adjacent frames to calculate bond switching was found to be large enough to allow for bond rotation and reconnection. 31,37

Machine Learning Classification. Following the procedure in ref 22 to build the input features of the SVM model, we first analyzed the local static, unstrained structure of the system. The output of the SVM model is determined from the spontaneous rearrangements of

the Al atoms under 300 K (in unstrained conditions). As such, the training data set used to train the SVM model is solely based on the thermal vibrations of nonstrained structures at 300 K.

In detail, the initially nonstrained configurations were equilibrated in the *NVT* ensemble at 300 K for 200 ps, while the trajectory was recorded for rearrangement analysis. In order to build up the SVM model without any prior knowledge of deformation, the rearrangements of each Al atom were calculated by the $p_{\rm hop}$ metric proposed by Candelier et $al.,^{56}$ which has been used extensively to identify rearrangements in amorphous materials. ^{22,57} To calculate $p_{\rm hop}$, we used a time scale $t_{\rm R}=6$ ps, which was found to be commensurate with the time required for rearrangements. For an atom at a given time frame t, two time intervals A and B are defined as $[t-t_{\rm R/2},t]$ and $[t,t+t_{\rm R/2}]$, respectively. Then $p_{\rm hop}$ of atom i at time t can be calculated as follows:

$$p_{\text{hop}}(t) = \sqrt{\langle (r_i - \langle r_i \rangle_{\text{B}})^2 \rangle_{\text{A}} \langle (r_i - \langle r_i \rangle_{\text{A}})^2 \rangle_{\text{B}}}$$
(3)

where $\langle \rangle_A$ and $\langle \rangle_B$ are averages over the time intervals A and B, respectively. When an atom is caged, $\langle r_i \rangle_A$ will approximately be equal to $\langle r_i \rangle_{\rm B}$, which will result in a $p_{\rm hop}$ value comparable to the scale of fluctuations within its cage. When p_{hop} exceeds a threshold value and exhibits a peak at a duration of time t, it represents that the particle has undergone a rearrangement. Here, we took the threshold value to be 0.2 Å², which was found to be large enough for identifying the rearrangement of the Al atoms (see Figure S22A). We find the same trend as in ref 22: that is, the accuracy of identifying mobile atoms will saturate when the threshold value is large enough. For example, when increasing the threshold to 0.5 Å², the accuracy can reach 0.85, but then the number of rearrangement events has decreased to around 700, which will negatively influence the generalization ability of the SVM model. After applying the threshold value of 0.2 Å² to all the investigated a-Al₂O₃ samples, we accumulated almost 8000 rearrangement events. Since most of the inert atoms have a $p_{
m hop}$ value below 0.05 (see Figure S22B), as also mentioned in ref 22, the nonrearrangement events are defined as those with $p_{\rm hop} < 0.05$. Meanwhile, we also randomly selected the same number (8000) of events without rearrangements.

The inputs in the SVM models are the descriptors of local structures of selected atoms. As described in ref 19, we used the same radial and angular structure functions to describe the local structure.

$$G(k; \mu) = \sum_{i} e^{-(r_{ik} - \mu)^{2}/L^{2}}$$
(4)

$$\Psi(k; \, \xi, \, \lambda, \, \zeta) = \sum_{i,j} e^{-(r_{ik}^{2} + r_{jk}^{2} + r_{ij}^{2})/\xi^{2}} (1 + \lambda \cos \theta_{ijk})^{\zeta}$$
(5)

Here, r_{ik} is the distance between atoms i and k and the range of μ values is selected to be between 0.6 and 10 Å, with an increment of 0.2 Å. The classification accuracy for different series of μ values is presented in Figure S23, showing that although the first peak of the Al–O radial function has the largest contribution, the long-range structure also influences the mobility of the atoms. The window parameter L was set to be 0.2 Å. θ_{ijk} is the angle between atoms i, j, and k. For the parameters ξ , λ , and ζ in the angular structure functions, we used a series of combinations to characterize different aspects of an atom's angular environment (see the values in ref 19).

On the basis of the structural descriptors and the corresponding labels (rearranging or nonrearranging), we then adopted the linear SVM algorithm by using the LIBSVM package⁵⁸ to train a classifier, which can be used to distinguish the rearranging and nonrearranging atoms based on their subsequent local environment. Consistent with the results of ref 19, we found the accuracy of the classifier to be insensitive to the regularization C parameter of SVM when C > 0.1. The cross-validation was carried out on random train/test splits while ensuring the independency of the training and test sets by avoiding the use of the same atoms in both the training and test processes. We also attempted to split the original data set based on time series, *i.e.*, 0-160 ps for training and 160-200 ps for testing, and this yielded a

similar accuracy result to that from the applied random splitting. After cross-validation, we used a C parameter of 1, which yielded accuracies of both the training and test sets of around 83%. The softness S_i of atom i is defined as the orthogonal distance between its position in the feature space and the SVM decision boundary hyperplane (see Figure 4A).

Finally, we also tested the generalization of the SVM model when trained on a partial data set. As shown in Table S1, we found that the generalization does not significantly decrease when using a partial data set for training and the rest for testing (decrease from 0.833 to 0.798). The worst case yields an accuracy of only 0.693 when using the 0 GPa data as training set and 4 GPa data as test set. This highlights the importance of including all the data sets to get the best prediction.

High-Mobility Cluster Analysis. Here, the Al atoms with high mobility were defined as Al atoms with the top 10% highest softness, which was defined dynamically at each strain step. We used the OVITO software 59 to visualize and perform a cluster analysis of a-Al₂O₃ configurations during tension. To this end, high-softness clusters were defined as a group of n Al atoms with high softness connected by O atoms, *i.e.*, when two Al atoms within a specified cutoff were considered to be connected. As shown above, the cluster analysis focused solely on the Al atoms. A cluster is defined as a group of n Al atoms within a cutoff of 3.7 Å, which is the minimum after the first peak in the Al–Al partial pair distribution function (see Figure S20B).

ASSOCIATED CONTENT

Solution Supporting Information

The Supporting Information is available free of charge at https://pubs.acs.org/doi/10.1021/acsnano.1c05619.

Additional data including the mechanical and structural properties of a-Al₂O₃; the evolution and distribution of bond switching activities; tuning of hyper parameters for the machine learning model; machine learning model performance with different features; correlations between softness and structural properties; and correlations between softness and dynamic properties (PDF)

AUTHOR INFORMATION

Corresponding Authors

Mathieu Bauchy — Physics of AmoRphous and Inorganic Solids Laboratory (PARISlab), Department of Civil and Environmental Engineering, University of California, Los Angeles, California 90095, United States; orcid.org/0000-0003-4600-0631; Email: bauchy@ucla.edu

Morten M. Smedskjaer – Department of Chemistry and Bioscience, Aalborg University, Aalborg 9220, Denmark; orcid.org/0000-0003-0476-2021; Email: mos@bio.aau.dk

Authors

Tao Du – Department of Chemistry and Bioscience, Aalborg University, Aalborg 9220, Denmark

Han Liu – Physics of AmoRphous and Inorganic Solids Laboratory (PARISlab), Department of Civil and Environmental Engineering, University of California, Los Angeles, California 90095, United States; orcid.org/ 0000-0002-4899-9998

Longwen Tang — Physics of AmoRphous and Inorganic Solids Laboratory (PARISlab), Department of Civil and Environmental Engineering, University of California, Los Angeles, California 90095, United States

Søren S. Sørensen – Department of Chemistry and Bioscience, Aalborg University, Aalborg 9220, Denmark; orcid.org/ 0000-0003-2230-7823 Complete contact information is available at: https://pubs.acs.org/10.1021/acsnano.1c05619

Author Contributions

M.M.S. conceived the study. T.D., M.M.S., and M.B. planned the computational work. T.D. performed the molecular dynamics simulations, structural analyses, and machine learning calculations, with assistance from H.L., L.T., and S.S.S. T.D. and M.M.S. wrote the manuscript, with revisions from M.B., L.T., S.S.S., and H.L. All authors participated in discussing the results.

Notes

The authors declare no competing financial interest.

ACKNOWLEDGMENTS

This work was supported by VILLUM FONDEN (grant no. 13253). We also thank Aalborg University for access to computational resources through CLAAUDIA. T.D. is supported by a Marie Skłodowska-Curie Individual Fellowship (101018156). M.B. acknowledges the support from the National Science Foundation under grants DMREF-1922167, CMMI-1762292, and CAREER-1944510.

REFERENCES

- (1) Lawn, B. R.; Swain, M. V. Microfracture Beneath Point Indentations in Brittle Solids. *J. Mater. Sci.* 1975, 10 (1), 113–122.
- (2) Griffith, A. A.; Taylor, G. I., VI The Phenomena of Rupture and Flow in Solids. *Philos. Trans. R. Soc. London. Ser. A* **1921**, 221, 163–198.
- (3) Yoshida, S. Indentation Deformation and Cracking in Oxide Glass Toward Understanding of Crack Nucleation. *J. Non-Cryst. Solids: X* **2019**, *1*, 100009.
- (4) Wondraczek, L.; Mauro, J. C.; Eckert, J.; Kühn, U.; Horbach, J.; Deubener, J.; Rouxel, T. Towards Ultrastrong Glasses. *Adv. Mater.* **2011**, 23 (39), 4578–4586.
- (5) Pineau, A.; Benzerga, A. A.; Pardoen, T. Failure of Metals I: Brittle and Ductile Fracture. *Acta Mater.* **2016**, *107*, 424–483.
- (6) Xi, X. K.; Zhao, D. Q.; Pan, M. X.; Wang, W. H.; Wu, Y.; Lewandowski, J. J. Fracture of Brittle Metallic Glasses: Brittleness or Plasticity. *Phys. Rev. Lett.* **2005**, 94 (12), 125510.
- (7) Schroers, J.; Johnson, W. L. Ductile Bulk Metallic Glass. *Phys. Rev. Lett.* **2004**, 93 (25), 255506.
- (8) Ketkaew, J.; Chen, W.; Wang, H.; Datye, A.; Fan, M.; Pereira, G.; Schwarz, U. D.; Liu, Z.; Yamada, R.; Dmowski, W.; Shattuck, M. D.; O'Hern, C. S.; Egami, T.; Bouchbinder, E.; Schroers, J. Mechanical Glass Transition Revealed by the Fracture Toughness of Metallic Glasses. *Nat. Commun.* **2018**, *9* (1), 3271.
- (9) Li, W.; Gao, Y.; Bei, H. On the Correlation between Microscopic Structural Heterogeneity and Embrittlement Behavior in Metallic Glasses. *Sci. Rep.* **2015**, *5* (1), 14786.
- (10) Yuan, F.; Huang, L. Brittle to Ductile Transition in Densified Silica Glass. Sci. Rep. 2014, 4 (1), 5035.
- (11) Greer, A. L.; Cheng, Y. Q.; Ma, E. Shear Bands in Metallic Glasses. *Mater. Sci. Eng.*, R **2013**, 74 (4), 71–132.
- (12) Cheng, Y. Q.; Ma, E. Atomic-Level Structure and Structure—Property Relationship in Metallic Glasses. *Prog. Mater. Sci.* **2011**, *56* (4), 379–473.
- (13) Nicolas, A.; Ferrero, E. E.; Martens, K.; Barrat, J.-L. Deformation and Flow of Amorphous Solids: Insights from Elastoplastic Models. *Rev. Mod. Phys.* **2018**, *90* (4), 045006.
- (14) Sollich, P.; Lequeux, F.; Hébraud, P.; Cates, M. E. Rheology of Soft Glassy Materials. *Phys. Rev. Lett.* **1997**, 78 (10), 2020–2023.
- (15) Argon, A. S. Plastic Deformation in Metallic Glasses. *Acta Metall.* 1979, 27 (1), 47–58.

- (16) Falk, M. L.; Langer, J. S. Dynamics of Viscoplastic Deformation in Amorphous Solids. *Phys. Rev. E: Stat. Phys., Plasmas, Fluids, Relat. Interdiscip. Top.* **1998**, *57* (6), 7192–7205.
- (17) Ding, J.; Patinet, S.; Falk, M. L.; Cheng, Y.; Ma, E. Soft Spots and Their Structural Signature in a Metallic Glass. *Proc. Natl. Acad. Sci. U. S. A.* **2014**, *111* (39), 14052–14056.
- (18) Richard, D.; Ozawa, M.; Patinet, S.; Stanifer, E.; Shang, B.; Ridout, S. A.; Xu, B.; Zhang, G.; Morse, P. K.; Barrat, J.-L.; Berthier, L.; Falk, M. L.; Guan, P.; Liu, A. J.; Martens, K.; Sastry, S.; Vandembroucq, D.; Lerner, E.; Manning, M. L. Predicting Plasticity in Disordered Solids from Structural Indicators. *Phys. Rev. Mater.* **2020**, *4* (11), 113609.
- (19) Cubuk, E. D.; Schoenholz, S. S.; Rieser, J. M.; Malone, B. D.; Rottler, J.; Durian, D. J.; Kaxiras, E.; Liu, A. J. Identifying Structural Flow Defects in Disordered Solids Using Machine-Learning Methods. *Phys. Rev. Lett.* **2015**, *114* (10), 108001.
- (20) Fan, Z.; Ma, E. Predicting Orientation-Dependent Plastic Susceptibility from Static Structure in Amorphous Solids *via* Deep Learning. *Nat. Commun.* **2021**, *12* (1), 1506.
- (21) Liu, H.; Xiao, S.; Tang, L.; Bao, E.; Li, E.; Yang, C.; Zhao, Z.; Sant, G.; Smedskjaer, M. M.; Guo, L.; Bauchy, M. Predicting the Early-Stage Creep Dynamics of Gels from Their Static Structure by Machine Learning. *Acta Mater.* **2021**, *210*, 116817.
- (22) Schoenholz, S. S.; Cubuk, E. D.; Sussman, D. M.; Kaxiras, E.; Liu, A. J. A Structural Approach to Relaxation in Glassy Liquids. *Nat. Phys.* **2016**, 12 (5), 469–471.
- (23) Bapst, V.; Keck, T.; Grabska-Barwińska, A.; Donner, C.; Cubuk, E. D.; Schoenholz, S. S.; Obika, A.; Nelson, A. W. R.; Back, T.; Hassabis, D.; Kohli, P. Unveiling the Predictive Power of Static Structure in Glassy Systems. *Nat. Phys.* **2020**, *16* (4), 448–454.
- (24) Cubuk, E. D.; Ivancic, R. J. S.; Schoenholz, S. S.; Strickland, D. J.; Basu, A.; Davidson, Z. S.; Fontaine, J.; Hor, J. L.; Huang, Y.-R.; Jiang, Y.; Keim, N. C.; Koshigan, K. D.; Lefever, J. A.; Liu, T.; Ma, X.-G.; Magagnosc, D. J.; Morrow, E.; Ortiz, C. P.; Rieser, J. M.; Shavit, A.; et al. Structure-Property Relationships from Universal Signatures of Plasticity in Disordered Solids. *Science* **2017**, 358 (6366), 1033–1037
- (25) Sharp, T. A.; Thomas, S. L.; Cubuk, E. D.; Schoenholz, S. S.; Srolovitz, D. J.; Liu, A. J. Machine Learning Determination of Atomic Dynamics at Grain Boundaries. *Proc. Natl. Acad. Sci. U. S. A.* **2018**, 115 (43), 10943–10947.
- (26) Sussman, D. M.; Schoenholz, S. S.; Cubuk, E. D.; Liu, A. J. Disconnecting Structure and Dynamics in Glassy Thin Films. *Proc. Natl. Acad. Sci. U. S. A.* **2017**, *114* (40), 10601–10605.
- (27) Freitas, R.; Reed, E. J. Uncovering the Effects of Interface-Induced Ordering of Liquid on Crystal Growth Using Machine Learning. *Nat. Commun.* **2020**, *11* (1), 3260.
- (28) de Pablo, J. J.; Jackson, N. E.; Webb, M. A.; Chen, L.-Q.; Moore, J. E.; Morgan, D.; Jacobs, R.; Pollock, T.; Schlom, D. G.; Toberer, E. S.; Analytis, J.; Dabo, I.; DeLongchamp, D. M.; Fiete, G. A.; Grason, G. M.; Hautier, G.; Mo, Y.; Rajan, K.; Reed, E. J.; Rodriguez, E.; et al. New Frontiers for the Materials Genome Initiative. npj Comput. Mater. 2019, 5 (1), 1–23.
- (29) van der Scheer, P.; van de Laar, T.; van der Gucht, J.; Vlassopoulos, D.; Sprakel, J. Fragility and Strength in Nanoparticle Glasses. ACS Nano 2017, 11 (7), 6755–6763.
- (30) Chatterjee, D.; Annamareddy, A.; Ketkaew, J.; Schroers, J.; Morgan, D.; Voyles, P. M. Fast Surface Dynamics on a Metallic Glass Nanowire. *ACS Nano* **2021**, *15* (7), 11309–11316.
- (31) Luo, J.; Wang, J.; Bitzek, E.; Huang, J. Y.; Zheng, H.; Tong, L.; Yang, Q.; Li, J.; Mao, S. X. Size-Dependent Brittle-to-Ductile Transition in Silica Glass Nanofibers. *Nano Lett.* **2016**, *16* (1), 105–113.
- (32) Zhang, Y.; Huang, L.; Shi, Y. Silica Glass Toughened by Consolidation of Glassy Nanoparticles. *Nano Lett.* **2019**, *19* (8), 5222–5228.
- (33) Zheng, K.; Wang, C.; Cheng, Y.-Q.; Yue, Y.; Han, X.; Zhang, Z.; Shan, Z.; Mao, S. X.; Ye, M.; Yin, Y.; Ma, E. Electron-Beam-

- Assisted Superplastic Shaping of Nanoscale Amorphous Silica. *Nat. Commun.* **2010**, *1* (1), 24.
- (34) Yang, Y.; Kushima, A.; Han, W.; Xin, H.; Li, J. Liquid-Like, Self-Healing Aluminum Oxide during Deformation at Room Temperature. *Nano Lett.* **2018**, *18*, 2492.
- (35) García Ferré, F.; Bertarelli, E.; Chiodoni, A.; Carnelli, D.; Gastaldi, D.; Vena, P.; Beghi, M. G.; Di Fonzo, F. The Mechanical Properties of a Nanocrystalline Al2O3/a-Al2O3 Composite Coating Measured by Nanoindentation and Brillouin Spectroscopy. *Acta Mater.* **2013**, *61* (7), 2662–2670.
- (36) Calvié, E.; Joly-Pottuz, L.; Esnouf, C.; Clément, P.; Garnier, V.; Chevalier, J.; Jorand, Y.; Malchère, A.; Epicier, T.; Masenelli-Varlot, K. Real Time TEM Observation of Alumina Ceramic Nano-Particles during Compression. *J. Eur. Ceram. Soc.* **2012**, 32 (10), 2067–2071.
- (37) Frankberg, E. J.; Kalikka, J.; Ferré, F. G.; Joly-Pottuz, L.; Salminen, T.; Hintikka, J.; Hokka, M.; Koneti, S.; Douillard, T.; Saint, B. L.; Kreiml, P.; Cordill, M. J.; Epicier, T.; Stauffer, D.; Vanazzi, M.; Roiban, L.; Akola, J.; Fonzo, F. D.; Levänen, E.; Masenelli-Varlot, K. Highly Ductile Amorphous Oxide at Room Temperature and High Strain Rate. *Science* **2019**, *366* (6467), 864–869.
- (38) van der Rest, A.; Idrissi, H.; Henry, F.; Favache, A.; Schryvers, D.; Proost, J.; Raskin, J.-P.; Van Overmeere, Q.; Pardoen, T. Mechanical Behavior of Ultrathin Sputter Deposited Porous Amorphous Al₂O₃ Films. *Acta Mater.* **2017**, *125*, 27–37.
- (39) Mercier, D.; Mandrillon, V.; Parry, G.; Verdier, M.; Estevez, R.; Bréchet, Y.; Maindron, T. Investigation of the Fracture of Very Thin Amorphous Alumina Film during Spherical Nanoindentation. *Thin Solid Films* **2017**, *638*, 34–47.
- (40) Jen, S.-H.; Bertrand, J. A.; George, S. M. Critical Tensile and Compressive Strains for Cracking of Al_2O_3 Films Grown by Atomic Layer Deposition. *J. Appl. Phys.* **2011**, *109* (8), 084305.
- (41) To, T.; Sørensen, S. S.; Christensen, J. F. S.; Christensen, R.; Jensen, L. R.; Bockowski, M.; Bauchy, M.; Smedskjaer, M. M. Bond Switching in Densified Oxide Glass Enables Record-High Fracture Toughness. *ACS Appl. Mater. Interfaces* **2021**, *13* (15), 17753–17765.
- (42) Tang, L.; Liu, H.; Ma, G.; Du, T.; Mousseau, N.; Zhou, W.; Bauchy, M. The Energy Landscape Governs Ductility in Disordered Materials. *Mater. Horiz.* **2021**, *8*, 1242.
- (43) Zhao, C.; Zhou, W.; Zhou, Q.; Zhang, Y.; Liu, H.; Sant, G.; Liu, X.; Guo, L.; Bauchy, M. Precipitation of Calcium—Alumino—Silicate—Hydrate Gels: The Role of the Internal Stress. *J. Chem. Phys.* **2020**, 153 (1), 014501.
- (44) Januchta, K.; Youngman, R. E.; Goel, A.; Bauchy, M.; Logunov, S. L.; Rzoska, S. J.; Bockowski, M.; Jensen, L. R.; Smedskjaer, M. M. Discovery of Ultra-Crack-Resistant Oxide Glasses with Adaptive Networks. *Chem. Mater.* **2017**, 29 (14), 5865–5876.
- (45) Plimpton, S. Fast Parallel Algorithms for Short-Range Molecular Dynamics. J. Comput. Phys. 1995, 117 (1), 1–19.
- (46) Matsui, M. A. Transferable Interatomic Potential Model for Crystals and Melts in the System CaO-MgO-Al₂O₃-SiO₂. *Mineral. Mag.* **1994**, *58A*, 571–572.
- (47) Ahuja, R.; Belonoshko, A. B.; Johansson, B. Melting and Liquid Structure of Aluminum Oxide Using a Molecular-Dynamics Simulation. *Phys. Rev. E: Stat. Phys., Plasmas, Fluids, Relat. Interdiscip. Top.* **1998**, *57* (2), 1673–1676.
- (48) Gutiérrez, G.; Belonoshko, A. B.; Ahuja, R.; Johansson, B. Structural Properties of Liquid Al₂O₃: A Molecular Dynamics Study. *Phys. Rev. E: Stat. Phys., Plasmas, Fluids, Relat. Interdiscip. Top.* **2000**, 61 (3), 2723–2729.
- (49) Gutiérrez, G.; Johansson, B. Molecular Dynamics Study of Structural Properties of Amorphous Al₂O₃. *Phys. Rev. B: Condens. Matter Mater. Phys.* **2002**, 65 (10), 104202.
- (50) Hockney, R. W.; Eastwood, J. W. Computer Simulation Using Particles; Taylor and Francis: New York, 1988.
- (51) Maloney, C. E.; Lemaître, A. Amorphous Systems in Athermal, Quasistatic Shear. *Phys. Rev. E* **2006**, 74 (1), 016118.
- (52) Thompson, A. P.; Plimpton, S. J.; Mattson, W. General Formulation of Pressure and Stress Tensor for Arbitrary Many-Body

- Interaction Potentials under Periodic Boundary Conditions. J. Chem. Phys. 2009, 131 (15), 154107.
- (53) Egami, T. Atomic Level Stresses. Prog. Mater. Sci. 2011, 56 (6), 637–653.
- (54) Zhou, Q.; Wang, M.; Guo, L.; Boolchand, P.; Bauchy, M. Intermediate Phase in Calcium—Silicate—Hydrates: Mechanical, Structural, Rigidity, and Stress Signatures. *Front. Mater.* **2019**, *6*, 157 DOI: 10.3389/fmats.2019.00157.
- (55) Du, T.; Li, H.; Sant, G.; Bauchy, M. New Insights into the Sol—Gel Condensation of Silica by Reactive Molecular Dynamics Simulations. *J. Chem. Phys.* **2018**, *148* (23), 234504.
- (56) Candelier, R.; Widmer-Cooper, A.; Kummerfeld, J. K.; Dauchot, O.; Biroli, G.; Harrowell, P.; Reichman, D. R. Spatiotemporal Hierarchy of Relaxation Events, Dynamical Heterogeneities, and Structural Reorganization in a Supercooled Liquid. *Phys. Rev. Lett.* **2010**, *105* (13), 135702.
- (57) Smessaert, A.; Rottler, J. Distribution of Local Relaxation Events in an Aging Three-Dimensional Glass: Spatiotemporal Correlation and Dynamical Heterogeneity. *Phys. Rev. E* **2013**, 88 (2), 022314.
- (58) Chang, C.-C.; Lin, C.-J. LIBSVM: A Library for Support Vector Machines. ACM Trans. Intell. Syst. Technol. 2011, 2 (3), 1–27.
- (59) Stukowski, A. Visualization and Analysis of Atomistic Simulation Data with OVITO—The Open Visualization Tool. *Modell. Simul. Mater. Sci. Eng.* **2010**, *18* (1), 015012.